

Article

Modeling and Control of IPMC-Based Artificial Eukaryotic Flagellum Swimming Robot: Distributed Actuation

José Emilio Traver *, Cristina Nuevo-Gallardo *, Paloma Rodríguez, Inés Tejado  and Blas M. Vinagre 

Escuela de Ingenierías Industriales, Universidad de Extremadura, Avda. de Elvas s/n, 06006 Badajoz, Spain; palomard@unex.es (P.R.); itejbal@unex.es (I.T.); bvinagre@unex.es (B.M.V.)

* Correspondence: jetraverb@unex.es (J.E.T.); cnuevog@unex.es (C.N.-G.)

Abstract: Ionic polymer-metal composites (IPMCs) are electrically driven materials that undergo bending deformations in the presence of relatively low external voltages, exhibiting a great potential as actuators in applications in soft robotics, microrobotics, and bioengineering, among others. This paper presents an artificial eukaryotic flagellum (AEF) swimming robot made up of IPMC segments for the study of planar wave generation for robot propulsion by single and distributed actuation, i.e., considering the first flagellum link as an actuator or all of them, respectively. The robot comprises three independent and electrically isolated actuators, manufactured over the same 10 mm long IPMC sheet. For control purposes, a dynamic model of the robot is firstly obtained through its frequency response, acquired by experimentally measuring the flagellum tip deflection thanks to an optical laser meter. In particular, two structures are considered for such a model, consisting of a non-integer order integrator in series with a resonant system of both non-integer and integer order. Secondly, the identified models are analyzed and it is concluded that the tip displacement of each actuator or any IPMC point is characterized by the same dynamics, which remains unchanged through the link with mere variations of the gain for low-frequency applications. Based on these results, a controller robust to gain variations is tuned to control link deflection regardless of link length and enabling the implementation of a distributed actuation with the same controller design. Finally, the deflection of each link is analyzed to determine whether an AEF swimming robot based on IPMC is capable of generating a planar wave motion by distributed actuation.

Keywords: swimming robot; ionic polymer-metal composite; fractional calculus; modeling; control



Citation: Traver, J.E.; Nuevo-Gallardo, C.; Rodríguez, P.; Tejado, I.; Vinagre, B.M. Modeling and Control of IPMC-Based Artificial Eukaryotic Flagellum Swimming Robot: Distributed Actuation. *Algorithms* **2022**, *15*, 181. <https://doi.org/10.3390/a15060181>

Academic Editor: Ramiro Barbosa and Isabel Jesus

Received: 1 May 2022
Accepted: 20 May 2022
Published: 25 May 2022

Publisher's Note: MDPI stays neutral with regard to jurisdictional claims in published maps and institutional affiliations.



Copyright: © 2022 by the authors. Licensee MDPI, Basel, Switzerland. This article is an open access article distributed under the terms and conditions of the Creative Commons Attribution (CC BY) license (<https://creativecommons.org/licenses/by/4.0/>).

1. Introduction

In recent decades, technological advances in micro and nanotechnology have opened up new lines of research. The field of microrobotics has received great attention due to the possibility of manufacturing tiny devices, which offers many and diverse applications, mainly derived from the ability to access small spaces at the microscale. Concretely, tiny artificial devices propelled on liquid environments (TADPOLES) can perform medical procedures in a minimally invasive way, deliver drugs with high precision, and detect towards diagnosis and monitoring, among other tasks [1–9]. However, the number of challenges increases as the working scale is scaled down, starting from fabrication techniques, power supply, as well as ways to propel such a kind of devices [6,10–17]. Therefore, a deep understanding of physics principles is fundamental for the design, manipulation, and control since the conventional consideration cannot be applied to the dynamic study of TADPOLES: they have to work within environments characterized by a low Reynolds number (Re , which is a dimensionless parameter that quantifies the ratio between inertial and viscous forces in a fluid), i.e., within environments dominated by viscous forces. In this regime, the study of swimmers' dynamics acquires an important role in understanding the motion and finding new ways for propulsion. A review on the theoretical framework for locomotion at low Re can be found in [18,19].

The analysis of the methods of propulsion at low Re inspired by biological systems has been extensively addressed in the literature from different perspectives. Considering only those focused on the well-known Purcell's swimmers, approaches based on motion primitives and resistive forces were reported in [20–24]. Other approaches propose the generation of planar waves by means of an eukaryotic flagellum applying the following methods: (1) by active distributed actuation [25–28]; (2) by two-point actuation [29,30]; (3) by single-point actuation with the absorption of the reflected wave [29,30]; and (4) by single-point actuation with a non-uniform distribution of mass (passive distributed actuation) [31–33].

However, the number of studies that analyze and implement these ways of propelling with a single material piece that can be found in the literature is limited. In this sense, the ionic polymer-metal composite (IPMC) is presented as an emerging material whose properties can fill this gap due to the possibility of both bending with a relatively low power supply (4–6 V) and underwater actuation, which makes it suitable for the development of swimming microrobots and biomedical applications. Nevertheless, the main works reported in robotics use IPMC as a simple actuator, with the robot body being made of other materials [34–39]. On the other hand, working with IPMCs involves a great number of challenges, beginning with fabrication techniques, as well as behavior characterization and performance analysis for control, which requires understanding the physical models, as well as the influence of physical parameters [40,41]. In this regard, different models describing the behavior of IPMC actuators have been reported, of integer [42] and non-integer orders consisting of two fractional poles and a fractional integrator [43].

In this context, this paper presents the first steps to propel a small-scale three-link artificial eukaryotic flagellum (AEF) swimming robot manufactured from a single IPMC sheet, where the three IPMC segments allow to actuate the flagellum in two ways: distributed, being the three segments active, or by single actuation, where only the first one is an actuator and the other two perform as passive links. Firstly, the robot modeling is addressed in the frequency domain to determine whether a single actuation is sufficient to generate a planar waveform, a motion that is necessary for robot propulsion in low Re . In particular, models consisting of a non-integer order integrators in series with a resonant system of both non-integer and integer order are considered in this work. To obtain the frequency responses experimentally, the first IPMC link actuator was attached to a couple of gold electrodes and the tip deflection of the third link was measured by means of a laser distance meter. Secondly, a robust controller is designed to control the tip displacement of each link in order to generate a non-reciprocal motion for propulsion. Finally, the deflection of each link is analyzed to determine whether an AEF swimming robot based on IPMC is capable of generating a planar wave motion by distributed actuation.

In summary, the two main contributions of this paper are: (1) fabrication of an IPMC-based AEF swimming robot; and (2) design of a controller robust to actuators of different lengths to propel the robot at low Re regimes. Hence, this article provides a different perspective from those presented in the aforementioned works, addressing the design of a small-scale swimming robot whose links are integrated into the same piece of material and can work as actuators or passive flexible links. In our previous works, an N -link AEF swimming robot with rotary joints was considered; the propulsion performance of such a kind of robot was studied (see [28] and references therein).

The contents of the paper are organized as follows. Section 2 briefly describes the mathematical background concerning the hydrodynamics of swimming robots at low Re environments, the types of waveforms for propulsion, and IPMC technology. Section 3 focuses on the IPMC-based AEF swimming robot, as well as the setup with which the experiments will be carried out. Section 4 contains the identification process performed to obtain an appropriate model of the robot for control purposes. The control design and simulations to analyze the motion of the swimming robot are approached in Section 5. Finally, Section 6 draws the concluding remarks and perspectives on the future work.

2. Background

This section describes the hydrodynamics of swimmers whose size is within the micrometer scale, i.e., working in low Re environments. A summary of the propulsion waveforms of an AEF swimming robot is also addressed. Likewise, a brief introduction to IPMC technology is given.

2.1. Hydrodynamics

When the swimming robot size ranges from milli to micrometers, the forces that predominate in the environment change as a consequence of the scale: inertial forces begin to lose importance in contrast to the viscous ones, which can be described by a low Re regime [14–16,44–46]. For this regime, the well-known Navier–Stokes equations reduce to Stokes’ equations as follows:

$$\begin{aligned} \mu \nabla^2 \mathbf{v} &= \nabla p \\ \nabla \cdot \mathbf{v} &= 0 \end{aligned} \tag{1}$$

where \mathbf{v} is the fluid velocity field, ∇p is the pressure gradient present in the fluid, and $\mu \nabla^2 \mathbf{v}$ represents the diffusion and internal forces. The first consequence of low Re regime governed by the Stokes’ equations is the reversibility of a flow, which implies that the motion of the fluid particles is independent of time and is the only function of the followed path. Therefore, according to the “scallop theorem” [47], a swimmer achieves zero net displacements when moving to a position and then returning by reversing the same sequence of movements and, as a consequence, a non-reciprocal motion is required to accomplish a net displacement different from zero. The difference between reciprocal and non-reciprocal motion is illustrated in Figure 1 by means of the simplest swimming robot, namely the so-called Purcell’s three-link swimmer. For the green-red arrow path, which corresponds to a reciprocal motion, the sequence of movements repeats step ‘B’ to complete the cycle. Therefore, the displacement achieved from A-B-C movements is canceled with C-B-A, since it is the same motion in opposite direction. On the other hand, the green-yellow arrow path shows a non-reciprocal motion as none of the steps is repeated, so all the movements contribute to robot displacement.

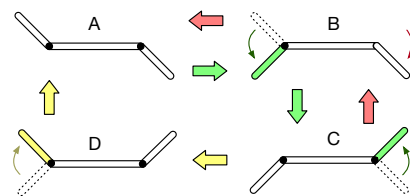


Figure 1. Graphical description of reciprocal (green-red arrow path, A-B-C-B-A) and non-reciprocal (green-yellow arrow path, A-B-C-D-A) motion with a Purcell’s swimming robot.

2.2. Waveforms

As mentioned above, the selection of an optimal non-reciprocal motion is a key factor in low Re environments, since the net displacement only depends on the geometrical sequence of movements [14,48]. In particular, planar waveforms describe a non-reciprocal motion. From a nature perspective, different kinds of waveforms can be observed in biological swimmers. The first kind is a planar (traveling) wave based on flagella of eukaryotic cells, which is described by a traveling harmonic wave [49]. Linear and quadratic traveling waves define the Carangiform fishes motion, i.e., the bending of their bodies in a propulsive wave that extends from head to tail end [50]. These three waveforms can be described by:

$$y(x, t) = (c_0 + c_1x + c_2x^2) \sin\left(\frac{2\pi}{\lambda}(x - V_pt)\right), \tag{2}$$

where c_0 , c_1 , and c_2 are the coefficients that govern the amplitude growth, x is the displacement along the propulsion axis, V_p refers to the propagation speed of the wave, and λ is the wavelength. For planar waves, the amplitude is only given by coefficient c_0 (the others are zero). For Carangiform swimmers, $c_0 = 0$. By choosing adequate values for coefficients c_1 and c_2 , two important properties for propulsion can be preserved: (1) the flagellum head is always maintained at zero amplitude (boundary condition, i.e., $y(0, t) = 0$), and (2) the wave amplitude along the flagellum can be modulated.

An alternative way for preserving such properties, which has been demonstrated to increase the forward propulsion velocity, is the use of a fractional growth for variable x as follows [28]

$$y(x, t) = (cx^\alpha) \sin\left(\frac{2\pi}{\lambda}(x - V_p t)\right), \quad (3)$$

where c defines the amplitude at the end of the flagellum, and $\alpha \in \mathbb{R}^+$ ($0 < \alpha < 1$) is the coefficient that determines the wave growth shape. In particular, when $\alpha = 0$, the resulting waveform is harmonic, whereas $\alpha = 1$ results in the Carangiform waveform. Thus, this waveform can be also viewed as a generalization of (2), merging the features from harmonic to Carangiform waveforms. Figure 2 depicts the four traveling waveforms described. Figure 2a illustrates the harmonic waveform, the linear waveform and the Carangiform waveform are depicted in Figure 2b, and the waveform with fractional growth for different values of α is shown in Figure 2c.

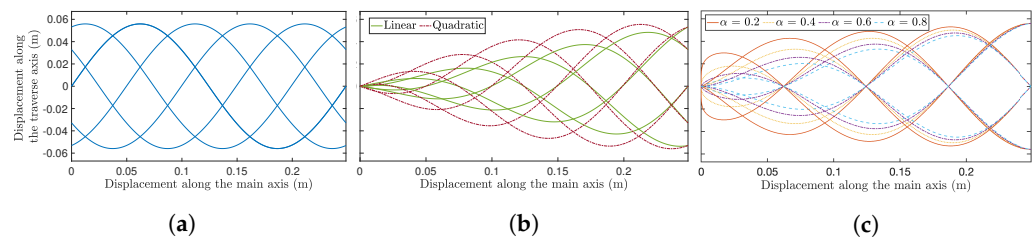


Figure 2. Appearance of the four different kinds of planar traveling waves: (a) harmonic waveform, (b) linear and quadratic Carangiform waveforms, (c) waveform with fractional growth.

2.3. IPMC Technology

IPMCs have received a significant amount of attention since they offer new opportunities for the development of flexible underwater robotic systems due to their intrinsic properties: large bending deformation under a low applied voltage (4–6 V), low density, and potential biocompatibility and biodegradability. They are usually manufactured by Nafion as the foundation polymer matrix, a thin ion-exchange layer based on a perfluorinated ionomer membrane in a hydrated state with water as a solvent, plated with platinum and attaching a couple of electrodes to both surfaces. The ion-exchange layer is neutralized with Na^+ counterions to balance the electric charge of the anions attached to the ionomer. Likewise, IPMC units can be also manufactured using different types of both ionomer membranes (such as Flemion) and counterions (such as Li^+ , Rb^+ or K^+) with water, ethylene glycol, or glycerol as solvent.

If a voltage is applied to one of the electrodes, an ion migration is produced, moving the hydrated cations and water molecules inside the polymer forward to the opposite surface. This motion will increase the gradient concentration, producing electrostatic and osmotic forces inside the polymer and forcing the bending as a result. Therefore, IPMCs are electrically driven materials that undergo bending deformations in the presence of external voltages.

3. Swimming Robot

This section focuses on the description of the AEF swimming robot manufactured by IPMC and the experimental setup used in this work.

3.1. Robot Description

Figure 3 shows the AEF swimming robot under study in this work. Inspired by the flagella of eukaryotic cells, the robot consists of three planar segments based on IPMC technology. The prototype was manufactured over the same IPMC sheet attending to the mechanical design in Figure 3a and the dimensions given in Table 1. For that purpose, a micro laser etching machine was used to cut the robot flagellum and isolate electrically each of the segments.

It is important to remark that each segment of the flagellum can behave as an independent actuator if it is electrically powered, or as a passive flexible link when it is not. In this work, only the first segment will be used as a robot actuator for robot modeling, so the rest of the links will behave as passive links. On the contrary, for control purposes, each link will be driven in order to reproduce a non-reciprocal motion for propulsion. The deflection of any of the links can be measured at its tip in both cases.

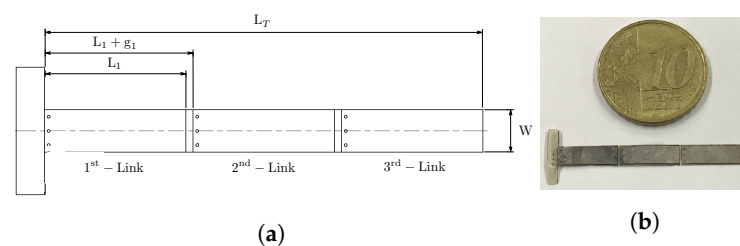


Figure 3. The three-link IPMC-based AEF swimming robot: (a) mechanical design, (b) image of the real prototype.

Table 1. Geometrical parameters of the IPMC-based AEF swimming robot.

Parameter	Description	Value	Unit
L_T	Length of robot	31	mm
W	Width of robot	3	mm
h	Thickness	250	μm
L_i	Length of actuator	10	mm
N	Number of links	3	-
g_l	Space between actuators	500	μm

3.2. Experimental Setup

The experimental setup used in this work for identification and control purposes of the manufactured swimming robot is illustrated in Figure 4a, which consists of:

- A water tank, used as an environment since the ultimate goal of the swimming robot is to be able to swim in a fluid.
- A laser distance meter (OADM 20U2441), to measure the deflection of the links.
- Gold electrodes, attached by means of a clamp, to transmit the voltage from the supplier to the IPMC surface.
- A USB multifunction I/O data acquisition board of National Instruments (NI-USB6259), which is connected to a computer in which LabVIEW™ 2020 SP1 runs to collect the data and generate the desired excitation voltage.
- A power stage, to provide sufficient power to the actuator from a power DC supplier and the desired voltage indicated by the computer.

Note that, although in the scheme only one laser meter is shown pointing to the end of the flagellum, there are two others to measure the deflection at the end of each of the other two segments, depending on the needs of the application to be developed. Likewise, other two additional pairs of electrodes are also available for distributed actuation.

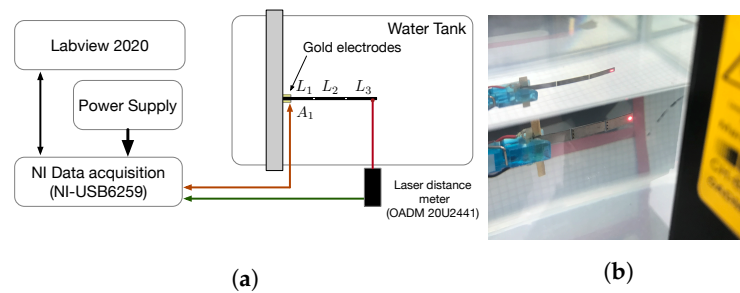


Figure 4. Experimental setup: (a) scheme, (b) swimming robot prototype pointed by the laser distance meter during an experiment.

The laser distance meter is calibrated for a resolution of 0.8 mm/V and pointed at the end of the desired link. Furthermore, the swimming robot is positioned in the middle of the range, allowing it to measure a maximum displacement of 4 mm. On the other hand, the voltage applied to the actuator is sampled with the USB multifunction I/O data acquisition board at a frequency of 1 kHz. Likewise, the output signal of the laser distance meter and the excitation voltage applied to IPMC are measured at the same sampling frequency and then sent to the computer in order to collect the data. Figure 4b shows a real image of the robot pointed by the laser during one of the experiments.

4. Robot Modeling

In this section, robot modeling is addressed in the frequency domain. The obtained results are discussed in order to determine what kind of actuation can be applied to the swimming robot to generate a planar waveform for propulsion.

4.1. Measuring Frequency Responses

The procedure described below was performed by measuring the deflection of each link and exciting exclusively the first actuator. To measure frequency responses, a frequency sweep is performed through a chirp signal with an amplitude of 3 V, a frequency range from 100 mHz to 200 Hz, and a duration of 200 s, with the objective of capturing all possible dynamics of the system and deciding which of them can be neglected for control purposes. The chirp signal is applied directly to the electrodes attached to the first actuator (A_1) and the system response is the deflection of the link under study. Figure 5 shows the excitation signal and the deflection measured at the third link (L_3). Likewise, every experiment was repeated 10 times in order to guarantee reproducibility and improve the final parameter estimation.

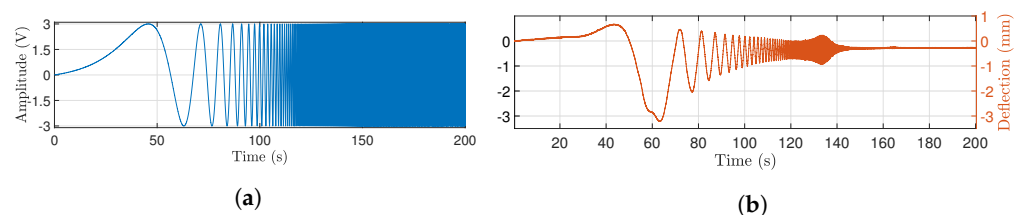


Figure 5. Example of experimental signals: (a) excitation signal applied to the first actuator for identification, (b) deflection measured on the third link.

The time response shows that the swimming robot reaches the relative maximum deflection in the resonance conditions and then decreases. Processing these data in MATLAB®, the frequency response was obtained using Welch's method dividing the set of data into eight sections with 50% overlap, each section was windowed with a Hamming window and the eight modified periodograms were computed and averaged. The average frequency response of the set of experiments obtained for each segment of the flagellum, 10 for each, is shown in Figure 6. Likewise, the maximum and minimum standard deviation is depicted for the response of the third link (gray lines).

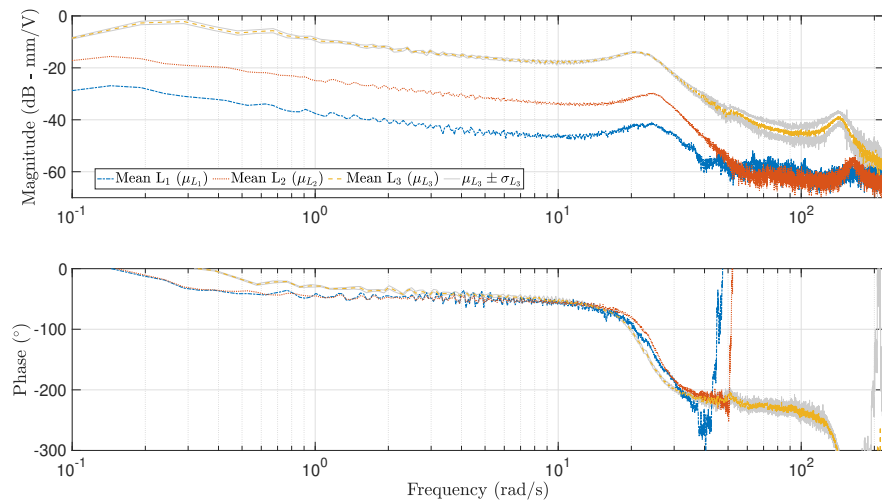


Figure 6. Frequency responses of the AEF swimming robot for the excitation of first segment and the deflection in each IPMC link.

4.2. Dynamic Model Identification

The theoretical models of IPMCs found in the literature stand out for their complexity and the huge variability of their chemical parameters due to the lack of technical standards in manufacturing methods. More precisely, the existing models can be categorized as: (1) black-box models, based on empirical responses [43]; (2) gray-box models, which combine the knowledge about materials with experimental data, i.e., they are formulated based on physical principles while empirical results are used to define more complex physical processes [42]; and (3) white-box models, whose components explain the physics and actuation responses by partial differential equations [51,52]. Taking into account that the last method is not practical for real-time control purposes due to the high computational efforts required, the second approach will be used in this work as described below.

From the measured frequency responses, it can be seen that the system has two resonance frequencies in the frequency range under study, regardless of the considered link. Moreover, the farther a link is from the first link, the lower the resonance peak. On the other hand, it should be remarked that the magnitude curves are not flat at low frequencies: they fall with a slope of -10 dB/dec being the phase approximately 45° . This behavior matches perfectly with a fractional integrator of order 0.5, i.e.:

$$H(s) \approx s^{-0.5} \quad (4)$$

It is worth mentioning that these low-frequency dynamics was also proved for other prototypes in [43,53,54], in our previous work [55], and in [42,51], whose theoretical models present root square of the Laplacian variable to define the electrical dynamics of IPMC.

Theoretical studies on IPMCs usually model mechanical behavior and hydrodynamic interactions when the actuator is submerged by coupling a resonant system for the first vibration mode in order to obtain a more reliable model. This consideration can be accepted in this work since, as it can be seen from the experimental frequency responses, the first resonance mode predominates for frequencies below 50 rad/s, which are high enough for the frequency range of interest for this application. Therefore, that dynamics may be given by a spring-mass-damper second order system of the form:

$$G_1(s) = \frac{a_0}{b_2s^2 + b_1s + 1} \quad (5)$$

or by a fractional order system as

$$G_2(s) = \frac{a_0}{b_1 s^\alpha + 1} \tag{6}$$

with $\alpha \in \mathbb{R}^+$ ($\alpha \in (1, 2)$), and being a_0 , b_1 , and b_2 constants. Notice that both models have the same number of parameters (i.e., three). Hence, the global dynamics of the system will be obtained as the fractional order integrator cascaded with the mechanical model, i.e., $P_i(s) = H(s)G_i(s)$, with $i = \{1, 2\}$, for the frequency range of interest of $[0.2, 50]$ rad/s.

For simplicity, the dynamics corresponding to the integrator was removed from the measured frequency responses. Consequently, the identification procedure was reduced to identify models of the form of (5) and (6) in the mentioned frequency range. In particular, the average frequency response of the 10 measurements was used for identification. Concerning the identification process, the Levy’s method is implemented in MATLAB® (with function `levy` [56]) for both the integer and the fractional order models. The adjustment was performed by minimizing $J = (G(j\omega)D(j\omega) - N(j\omega))^2$, i.e., the quadratic error per sampling frequency ($N(j\omega)$ and $D(j\omega)$ are the numerator and denominator of the transfer function of the model to be identified, respectively). Fractional models were found sweeping α in the interval $(1, 2)$, with a step of 0.01, and choosing the best result from among the stable models obtained.

The model parameters derived from the above-described identification process are indicated in Table 2. From these results, it can be stated that: (i) as expected, the two models $G_i(s)$ obtained for each link are stable; (ii) gains of the models (coefficient a_0) are of the same order of magnitude; and (iii) the values obtained for the parameter α for each of the models are very similar. Figure 7 shows a comparison of the experimental data and the frequency response of the identified model for each robot link (denoted as $P_{L_q}(j\omega) = H(j\omega)G_{1_{L_q}}(j\omega)$, being $L_q = \{L_1, L_2, L_3\}$ the link and $G_{1_{L_q}}(s)$ the dynamics of each link with the form of (5)). As can be observed, differences between experimental and model frequency responses appear at frequencies higher than 50 rad/s, i.e., outside of the range of interest.

In order to compare and evaluate the goodness of the obtained models, besides J , additional performance indices were calculated: mean square error (MSE), mean absolute deviation (MAD), maximum deviation (MD), and coefficient of determination R^2 , all of them calculated in the same way as in [55]. They are given in Table 3, where the best fits are in bold. To this respect, except for the third link, the best results are obtained using the model $G_1(s)$ given by (5). However, for the third link that model is also the best in terms of J and MD, but not if another of the remaining indices is considered.

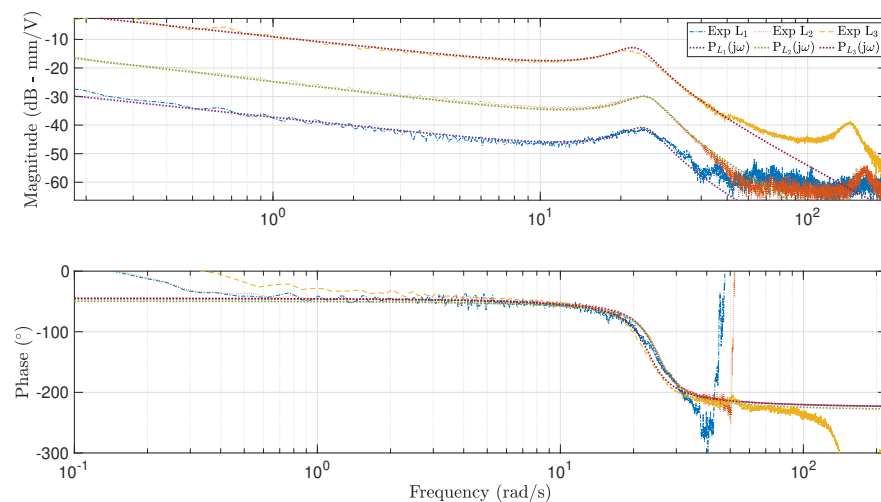


Figure 7. Comparison of experimental and model frequency responses of the AEF swimming robot by exciting the first actuator and measuring the deflection at the end of each link.

Table 2. Model parameters obtained from identification procedure.

Model	α	$a_0 (\times 10^{-3})$	$b_2 (\times 10^{-3})$	$b_1 (\times 10^{-3})$
First link	G_1	-	13.70	1.62
	G_2	1.79	13.33	-
Second link	G_1	-	51.00	1.61
	G_2	1.81	48.10	-
Third link	G_1	-	376.09	2.13
	G_2	1.71	352.80	-

Table 3. Performance indices after fitting models $P_1(s)$ and $P_2(s)$. Numbers in bold correspond to the best fit.

Model	$J (\times 10^{-5})$	MSE ($\times 10^{-7}$)	MAD ($\times 10^{-4}$)	MD ($\times 10^{-3}$)	R^2	
First link	P_1	2.4884	4.5210	5.4392	2.800	0.9153
	P_2	3.4992	5.0188	5.7149	3.3000	0.9059
Second link	P_1	4.9163	59.7630	13.0000	24.0000	0.9630
	P_2	12.3680	104.2300	19.0000	28.5000	0.9354
Third link	P_1	530.0000	1654.7000	69.0000	126.5000	0.9796
	P_2	550.0000	1392.7200	45.000	186.4000	0.9828

4.3. Discussion of the Results

According to the above results, it can be stated that the links have similar dynamics regardless of their position. However, there are differences in the gain, which means a greater displacement as the closer to the end of the flagellum is measured. Specifically, the tip displacement of the second link shows an increase in gain, whereas the tip displacement of the third link also presents a lag with respect to the first link as a consequence of the length, the flexible behavior of IPMC and the interaction with the environment. These conclusions are illustrated in Figure 8, which schematizes the relation between the first and the rest of the links. (At this point, it should be recalled that the first link is active, while the other two behave as passive links). The values of the gains and the phase lag of the third link can be directly deduced from Table 2 as follows: $K_2 = 3.72$, $K_3 = 7.37$, and $\phi = 4^\circ$. It should be noted that the gain does not increase linearly due to the fact that the IPMC bends into a C-shape, so the closer to the end is measured, the higher the displacement.

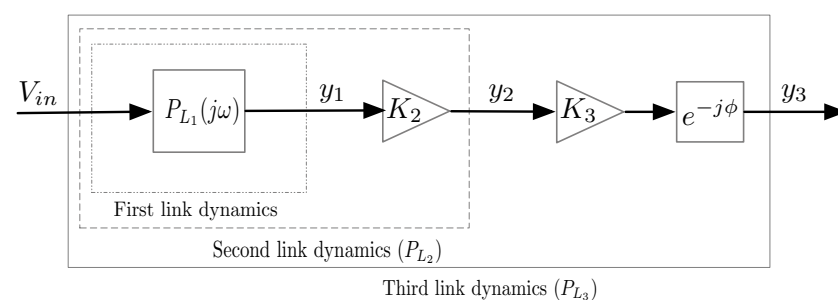


Figure 8. Diagram block of swimming robot model for single actuation.

Hence, it can be concluded that the displacement of the end of each flagellum segment, or of any IPMC point, is characterized by the same dynamics, which remains unchanged along with the link with mere variations of the gain for low-frequency applications. This conclusion is also consistent with other studies reported in the literature, where IPMCs show changes in model gain when the links do not have the same length or are manufactured from different substrates (see e.g., [31,41,43,55]).

Moreover, from the above conclusion, it can be stated that a non-reciprocal motion cannot be achieved with a single actuation if the geometrical and mechanical design of

the swimming robot has not been analyzed previously and designed for that purpose, otherwise the dynamics of consecutive links are subjected to the active link. In other words, it is not possible that the swimming robot carries out a non-reciprocal motion with a single actuation; a distributed actuation is needed to obtain the desired waveform and, consequently, for robot propulsion.

Finally, the dynamics considered for the control design is the one corresponding to the third link, which takes the form:

$$P_{L_3}(s) = \frac{1}{s^{0.5}} \frac{376.09 \times 10^{-3}}{2.13 \times 10^{-3}s^2 + 23.31 \times 10^{-3}s + 1} \quad (7)$$

It is worth mentioning that such a dynamics is considered because it represents the worst case: a further increase in the third link gain may cause the system to become unstable, as the gain variation is not linear; on the contrary, a decrease in gain does not compromise the stability of the system.

5. Robot Propulsion

This section addresses the motion control of the AEF swimming robot to reproduce the desired waveform. Firstly, the formulation of the problem under study is explained. Then, two controllers are tuned for robot propulsion, namely a traditional integer order proportional-integral-derivative (PID) and a fractional order integrator. Motion analysis when applying both controllers is then discussed.

5.1. Problem Formulation

Two main issues have to be addressed when trying to generate a non-reciprocal motion, especially a planar traveling wave. Firstly, the desired waveform must be adapted to the swimming robot dynamics and discretized for its geometry, considering that it is necessary to define a reference for each of the robot's links. This will fulfill the capabilities of the swimming robot in terms of amplitude and velocity. The resulting waves will be the references of the IPMC links. Secondly, a tracking controller needs to be applied to each link to follow the desired deflection.

The methodology applied to discretize the motion is based on [28], which divides the flagellum into the same number of segments and the same length as the swimming robot has, providing a matrix, $A[T][N]$, that contains the trajectory as a function of time and space for the N links of the robot. However, it should be noted that in this work the above method is modified to obtain the waveform amplitude instead of the link angle. The type of waveform chosen is the linear Carangiform, due to the physical limitations of IPMCs (slow dynamics and low amplitude responses). Therefore, the linear Carangiform waveform may be the most suitable for this type of material in contrast to other ones that require a greater range of motion, which means very low frequencies or the impossibility to perform the motion. The parameters that define the linear Carangiform motion according to the waveform expression (2) are collected in Table 4. With respect to the wavelength, it was defined using the criterion applied in [28], which means it is equal to the robot's length.

Table 4. Linear Carangiform waveform parameters.

Parameter	Value	Description	Unit
c_0	0	Amplitude coefficient	μm
c_1	200	Amplitude coefficient	-
c_2	0	Amplitude coefficient	$1/\mu\text{m}$
f	0.01	Frequency	Hz
λ	32	Wavelength	mm

In order to track the calculated references, as commented above, a controller for each link that takes the following considerations into account is required. Firstly, from the

identification procedure, it has been deduced that the dynamics of the IPMC links are very similar and that only variations in the gain are observed as a consequence of its strong dependence on the link length. Secondly, it has been found that an equal link length does not provide the optimal waveform and, consequently, the optimal drive for a given number of links [25]. With this motivation, a controller robust to variations in the system gain is considered to overcome the robot propulsion, so that it can also be applied after a link length optimization process.

5.2. Control Design

The methodology applied to design the controller is based on the reference model strategy proposed in [57], which adjusts the step response of the controlled system to an ideal closed-loop system. The frequency domain specifications for the ideal closed-loop are:

1. Gain crossover frequency: $\omega_{cg} = 5$ rad/s.
2. Phase margin: $\phi_m = 75^\circ$.

Based on the above specifications, the ideal Bode transfer function of a non-integer integrator is taken as the ideal reference model, whose open- and closed-loop forms are, respectively:

$$L_{ol}(s) = \left(\frac{\omega_c}{s}\right)^\gamma \quad (8)$$

$$L_{cl}(s) = \frac{1}{(s/\omega_c)^\gamma + 1} \quad (9)$$

where ω_c denotes the crossover frequency, and $\gamma \in (0, 2]$ is the non-integer order of the reference system. The gain and phase of the ideal reference model (8) are given by [57,58]:

$$|L_{ol}(j\omega)| = -20\gamma \log_{10} \left(\frac{\omega}{\omega_c}\right) \text{ dB/dec}$$

$$\arg[L_{ol}(j\omega)] = -\gamma\pi/2 \text{ rad}$$

The reference model has a constant phase at any frequency to ensure that the controlled system is robust to gain variations and exhibits an iso-damping property at a step response. Then, based on the above relationships, the system must have a crossover frequency of $\omega_c = \omega_{cg} = 5$ rad/s and a non-integer order of $\gamma = 1.16$ to meet the desired specifications.

In order to achieve this dynamics with the IPMC link model identified (Equation (7)), a PID controller is considered in parallel form as:

$$C_{PID}(s) = K_p + \frac{K_i}{s} + K_d s \quad (10)$$

where K_p , K_i , and K_d are the proportional, integral, and derivative gains, respectively. The controller parameters were determined by an optimization process based on the structure presented in [57], minimizing the following cost function:

$$J(K_p, K_i, K_d) = \int_0^\infty \left(\frac{1}{2} + \frac{t}{2}\right) |e(t)| dt = \int_0^\infty \left(\frac{1}{2} + \frac{t}{2}\right) |y_r(t) - y(t)| dt \quad (11)$$

where $y_r(t)$ is the desired output, obtained from the reference model, and $y(t)$ is the output of the controlled swimming robot link with the proposed controller. Note that cost function (11) is a combination of the integral time absolute error (ITAE), to evaluate the performance of the system over time (it penalizes the errors that are persistent and neglects the initial errors) [59], and the integral of absolute error (IAE), to quantify the performance to be sensitive at low errors [59].

The optimization process is divided into two steps and is carried out by combining both MATLAB[®] and Simulink[®]. The first step is to implement the system (the dynamics of the third link, i.e., model (7)) controlled by a PID, whose gains are variable, in closed-loop,

together with the scheme corresponding to the reference model. The second step is a MATLAB script that implements an iterative process based on the Nelder–Mead simplex search method, through the function `fminsearch`, that runs the mentioned Simulink model calculating the cost function J given by (11). In particular, this script varies the parameters of the PID controller until the values that minimize J are found, i.e., the controller optimal values. In order to be able to find a globally optimal solution, the iterative process was applied for a wide number of initial conditions, which were randomly changed for each optimization. The resulting optimal controller is the following:

$$C_{\text{PID}}(s) = 8.12 + \frac{53.36}{s} + 0.61s \quad (12)$$

It is worth mentioning that other performance indices were tried, but results with small variations were obtained with respect to the ones presented.

Upon analyzing the design method for the IPMC link model, which also contains non-integer order dynamics, the conclusion is drawn that the PID controller attempts to approximate the dynamics of a non-integer order integrator with the purpose of approaching the system to the desired dynamics. On this basis, a non-integer integrator is also considered for comparison purposes with the form:

$$C_I(s) = \frac{K}{s^\lambda} \quad (13)$$

where $\lambda \in (0, 1]$ is its order. Unlike PID, the parameters of fractional integrator are calculated analytically from the design specifications, which results in

$$C_I(s) = \frac{15.62}{s^{0.62}} \quad (14)$$

Moreover, this controller was approximated by the Oustaloup method with four poles and four zeros in the frequency range $[0.001, 100]$ rad/s as follows:

$$C_I^*(s) = \frac{32.08s^4 + 1981s^3 + 6511s^2 + 1196s + 11.7}{36.47s^4 + 372.9s^3 + 202.9s^2 + 6.175s + 0.01} \quad (15)$$

The Bode plots of the three designed controllers, namely $C_{\text{PID}}(s)$, $C_I(s)$, and $C_I^*(s)$, are shown in Figure 9. As can be seen, the PID controller provides a phase of 44° at 5 rad/s and a positive gain to the system at relatively high frequencies, which will increase the speed of the system, but at the same time, the crossover frequency specification will not be met. In contrast, the non-integer integrator has a bit higher phase at 5 rad/s, namely 56° , and a positive gain of 15 dB, so the design specifications can be better fulfilled. As for the approximation of the fractional integrator, it should be noted that it performs very close to $C_I(j\omega)$, with only a small variation in the phase from the desired ω_{cg} being observed.

Figure 10 illustrates Bode plots of the open-loop system when applying the designed controllers and the approximation. From these frequency responses, the first remark that can lay bare is that the PID controller does not meet the design specifications: as it was commented, the controller increases the speed of the system ($\omega_{cg} = 38$ rad/s) and the phase margin is 75° . The reason for the frequency response mismatch is due to the fact that the optimization process was approached from a time perspective, to adjust the time response of the system for a step input. On the contrary, the system fulfills the design specifications perfectly when applying a fractional order integrator. Furthermore, the phase is flat at crossover frequency and almost constant within an interval around it. In other words, the system is robust to gain variations and the overshoot of the response will be almost constant close to ω_{cg} .

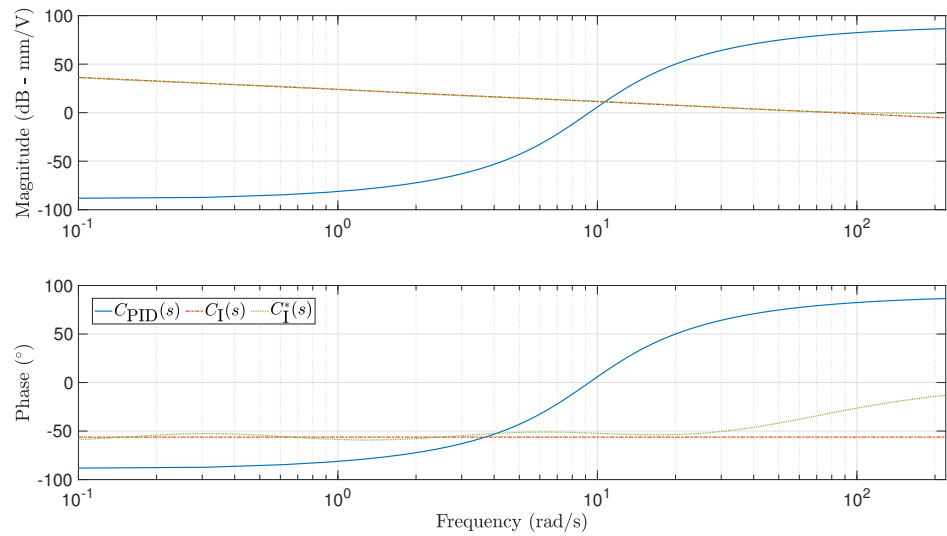


Figure 9. Frequency response of the designed integer and fractional order controllers.

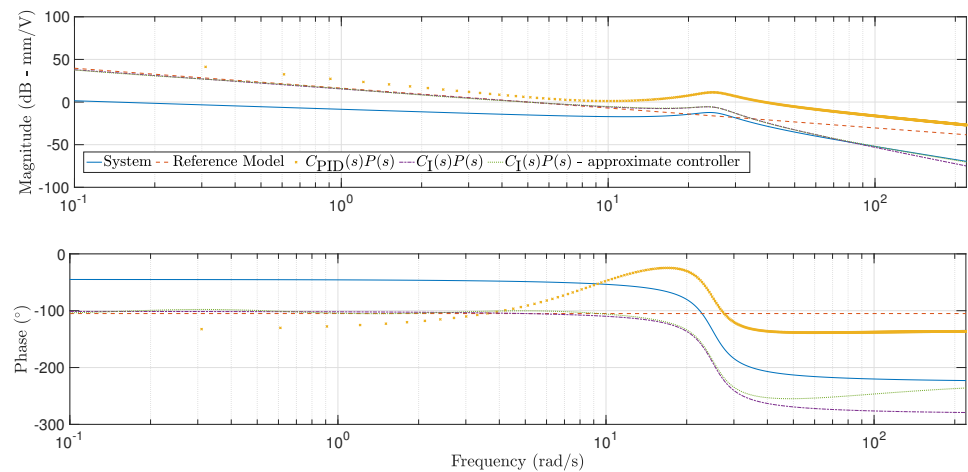


Figure 10. Frequency response of the reference model and the controlled system in open-loop.

The issues mentioned above can be also observed from the results plotted in Figure 11, which illustrates the step response of the reference model and that corresponding to each link of the robot when applying the PID (see Figure 11a) and the fractional integrator and its approximation (see Figure 11b). As far as the PID controller is concerned, the response for the third link shows a good fit with respect to the reference model response. However, the characteristics of this behavior do not hold for the other links: the overshoot increases as the gain decreases, although the system is faster for the second and third links compared to the other control strategy. This behavior is not observed in the system for the fractional integrator, which also approximates the step response of the reference model and, in the case of applying the controller to other links, the overshoot is maintained, ensuring robustness to gain variations. Regarding the integrator approach, the responses show small differences with respect to the ideal case, with the system velocity and overshoot remaining unchanged for all three links.

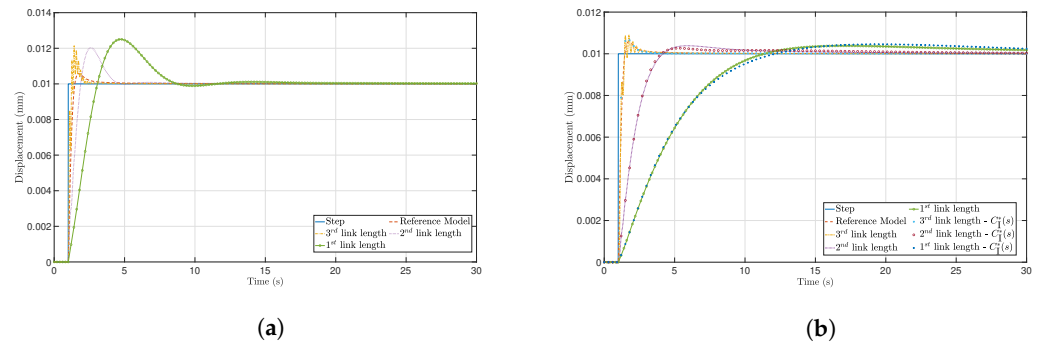


Figure 11. Step response of each robot link when applying: (a) PID controller, (b) non-integer order integrator and its approximation.

5.3. Motion Analysis

The swimming robot model was implemented in Simulink[®] on the basis of the description given in Section 4. Three equal IPMC links are concatenated and modeled with the same dynamics since they have the same length. Specifically, the link dynamics is defined as $P_{L_q}(s) = H(s)G_{1L_q}(s)$, where the model parameters of $G_{1L_q}(s)$ for each link are contained in Table 2. The total displacement of a link is calculated by means of its relative displacement and the angle of the previous link end.

Figure 12 shows the displacement of each link tracking its reference for the designed control strategies (see Figure 12a) and the comparison between the ideal linear Carangiform motion and the motion resulting from the distributed actuation (see Figure 12b). Firstly, let us comment on the results of Figure 12a. Independently of the flagellum segment, both controllers track closely the references, although the PID controller achieves better tracking as the controller increases the speed of the system. However, an increase in the tracking error is also observed as a consequence of the amplitude increase in the reference signal and the compensation of the dynamic motion of the previous link. In order to evaluate the tracking performance of the controllers, the ITAE and IAE indices were calculated. The results of the performance indexes obtained from the simulation are given in Table 5. It is important to remark that the results of the non-integer order controller correspond to its approximation. The indices validate the previous statement: the best performance is achieved in the first link, where the effort demanded by the reference is lower and the second and third links obtain worse tracking, although the error between them is similar, which shows the robustness of the controller. In addition, the PID controller exhibits a better tracking performance, although its behavior at step response is worse.

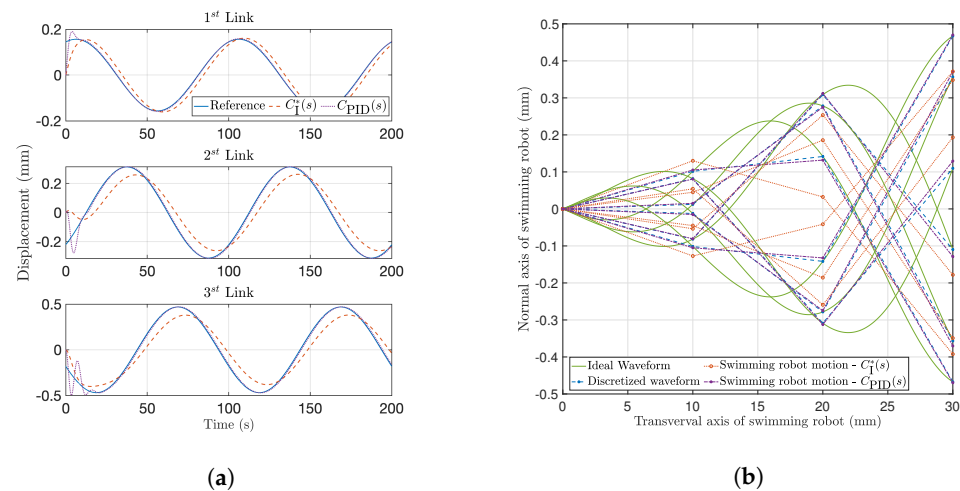


Figure 12. Swimming robot motion: (a) tracking results for the three robot links, (b) comparison of the ideal, discretized, and realized linear Carangiform waveform.

With respect to the results of Figure 12b, the ideal linear waveform, the discretized one obtained from the projection method described in [28] and the realized waveform are illustrated. As can be seen, the swimming robot is able to perform a non-reciprocal motion through a distributed actuation, although there exists a higher amplitude error and lag on the response when applying the fractional integrator, which will affect the robot's propulsion. The non-reciprocal motion for the ideal waveform and the obtained by applying each designed controller can be observed more clearly in Figure 13, which represents a three-dimensional graph showing time, the normal and transverse axis of the swimming robot. For the three cases, the ideal and simulated results show that the flagellum motions perform a wave that travels along the flagellum and over time.

Table 5. Tracking performance indices.

Link	IAE		ITAE	
	$C_I(s)$	$C_{PID}(s)$	$C_I(s)$	$C_{PID}(s)$
First link	4.67	0.68	434.90	42
Second link	13.87	2.28	1283.50	140.75
Third link	18.04	3.97	1861.70	269.74

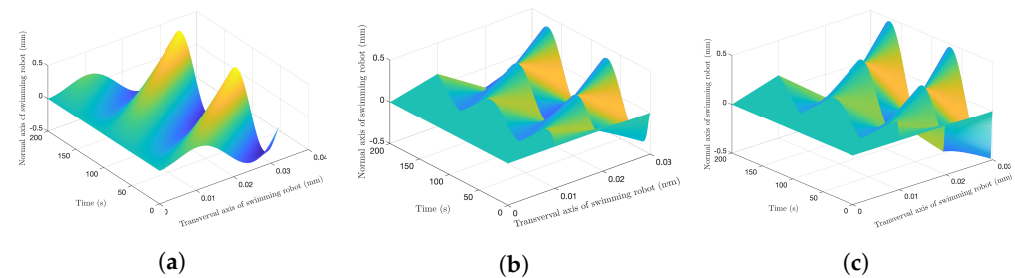


Figure 13. Three-dimensional representation of non-reciprocal motion for: (a) ideal waveform, (b) simulated motion with $C_{PID}(s)$, (c) simulated motion with $C_I^*(s)$.

6. Conclusions

In this paper, an artificial eukaryotic flagellum (ABF) swimming robot made up of ionic polymer-metal composite (IPMC) has been studied for the generation of planar traveling waves through single and distributed actuation in low Reynolds number (Re) environments. The robot comprised three independent and electrically isolated actuators manufactured over the same 10 mm long IPMC sheet.

Firstly, the swimming robot dynamics was identified for control purposes through its frequency response. It was obtained experimentally in LabVIEW by attaching a couple of gold electrodes to the first actuator and measuring the tip deflection by means of a laser distance meter. The experiments were performed considering the first segment as actuator and the rest acting as passive flexible links, and the deflection of each of the links was measured. Models consisting of a fractional integrator in series with a resonant system of both fractional and integer order were identified in the frequency range $[0.1, 50]$ rad/s for each link. The results showed that both models can be adequate for control purposes. Furthermore, the identification process led to the conclusion that the tip displacement and of any IPMC point are characterized by the same dynamic, which remains unchanged along with the link with mere variations of the gain for low-frequency applications. From this conclusion, it was also deduced that single actuation of the robot does not allow to produce a non-reciprocal motion, since the dynamics of the second and third links are subject to the dynamics of the first link. There are only differences in the gain and a slight phase lag, which are not sufficient to generate a non-reciprocal motion.

Secondly, a controller robust to gain variations was designed to control link deflection regardless of link length allowing to address a distributed actuation with the same controller design. It was tuned based on the methodology of the reference model and two control

strategies were proposed: a classical proportional-integral-derivative (PID) controller and a non-integer order integrator. The results showed that the PID offers a better response to tracking control as a consequence of the increased system speed, but does not meet the design specifications. In contrast, the non-integer order integrator meets the step response specifications but provides worse results for the tracking problem. Finally, the motions of the AEF swimming robot composed of three links of the same length were analyzed to validate that the robot performs a non-reciprocal motion, determining that a distributed actuation generates a planar wave motion. Therefore, it was also concluded that a distributed actuation (active or passive) is necessary to develop a non-reciprocal motion.

Our future works will focus on: (1) validating the distributed actuation method in the real prototype; and (2) studying the control approach for a swimming robot with segments of different lengths designed to optimize robot propulsion.

Author Contributions: This work involved all coauthors. Conceptualization, I.T. and B.M.V.; Formal analysis, J.E.T.; Investigation, J.E.T. and P.R.; Project administration, I.T. and B.M.V.; Writing—original draft, J.E.T.; Writing—review and editing, C.N.-G., I.T. and B.M.V. All authors have read and agreed to the published version of the manuscript.

Funding: This work was supported in part by the Consejería de Economía, Ciencia y Agenda Digital (Junta de Extremadura) under the project IB18109 and the grant “Ayuda a Grupos de Investigación de Extremadura” (no. GR21168), by the Agencia Estatal de Investigación (Ministerio de Ciencia e Innovación) through the project PID2019-111278RB-C22/AEI/10.13039/501100011033, and in part by the European Regional Development Fund “A way to make Europe”.

Data Availability Statement: Data will be made available on request.

Acknowledgments: José Emilio Traver would like to thank the Ministerio de Educación, Cultura y Deporte its support through the scholarship no. FPU16/2045 of the FPU Program. The authors would like to thank S. Hassan HosseinNia and Andres Hunt at the Technical University of Delft, The Netherlands, where the swimming robot was fabricated.

Conflicts of Interest: The authors declare no conflicts of interest.

Abbreviations

The following abbreviations are used in this manuscript:

AEF	Artificial eukaryotic flagellum
IPMC	Ionic polymer-metal composite
PID	Proportional-integral-derivative
MAD	Mean absolute deviation
MD	Maximum deviation
MSE	Mean square error
R ²	Coefficient of determination
Re	Reynolds number
TADPOLE	Tiny artificial devices propelled on liquid environments

References

1. Sitti, M.; Ceylan, H.; Hu, W.; Giltinan, J.; Turan, M.; Yim, S.; Diller, E. Biomedical Applications of Untethered Mobile Milli/Microrobots. *Proc. IEEE* **2015**, *103*, 205–224. [[CrossRef](#)]
2. Li, J.; Esteban-Fernández de Ávila, B.; Gao, W.; Zhang, L.; Wang, J. Micro/nanorobots for biomedicine: Delivery, surgery, sensing, and detoxification. *Sci. Robot.* **2017**, *2*, eaam6431. [[CrossRef](#)]
3. Medina-Sánchez, M.; Xu, H.; Schmidt, O.G. Micro- and nano-motors: The new generation of drug carriers. *Ther. Deliv.* **2018**, *9*, 303–316. [[CrossRef](#)]
4. Soto, F.; Wang, J.; Ahmed, R.; Demirci, U. Medical micro/nanorobots in precision medicine. *Adv. Sci.* **2020**, *7*, 2002203. [[CrossRef](#)]
5. Arvidsson, R.; Hansen, S.F. Environmental and health risks of nanorobots: An early review. *Environ. Sci. Nano* **2020**, *7*, 2875–2886. [[CrossRef](#)]
6. Wu, Z.; Chen, Y.; Mukasa, D.; Pak, O.S.; Gao, W. Medical micro/nanorobots in complex media. *Chem. Soc. Rev.* **2020**, *49*, 8088–8112. [[CrossRef](#)]

7. Fu, S.; Wei, F.; Yin, C.; Yao, L.; Wang, Y. Biomimetic soft micro-swimmers: From actuation mechanisms to applications. *Biomed. Microdevices* **2021**, *23*, 6. [[CrossRef](#)]
8. Sun, B.; Wood, G.; Miyashita, S. Milestones for autonomous in vivo microrobots in medical applications. *Surgery* **2021**, *169*, 755–758. [[CrossRef](#)]
9. Jiang, J.; Yang, Z.; Ferreira, A.; Zhang, L. Control and autonomy of microrobots: Recent progress and perspective. *Adv. Intell. Syst.* **2022**. [[CrossRef](#)]
10. Shimoyama, I. Scaling in microrobots. In Proceedings of the 1995 IEEE/RSJ International Conference on Intelligent Robots and Systems. Human Robot Interaction and Cooperative Robots, Pittsburgh, PA, USA, 5–9 August 1995; Volume 2, pp. 208–211.
11. Trimmer, W.; Jebens, R. Actuators for micro robots. In Proceedings of the 1989 IEEE International Conference on Robotics and Automation, Scottsdale, AZ, USA, 14–19 May 1989; pp. 1547–1548.
12. Wautelet, M. Scaling laws in the macro-, micro- and nanoworlds. *Eur. J. Phys.* **2001**, *22*, 601–611. [[CrossRef](#)]
13. Abbott, J.J.; Nagy, Z.; Beyeler, F.; Nelson, B.J. Robotics in the small, part I: Microbotics. *IEEE Robot. Autom. Mag.* **2007**, *14*, 92–103. [[CrossRef](#)]
14. Lauga, E.; Powers, T.R. The hydrodynamics of swimming microorganisms. *Rep. Prog. Phys.* **2009**, *72*, 096601. [[CrossRef](#)]
15. Diller, E.; Sitti, M. Micro-scale mobile robotics. *Found. Trends Robot.* **2013**, *2*, 143–259. [[CrossRef](#)]
16. Sitti, M. *Mobile Microrobotics*; MIT Press: Cambridge, MA, USA, 2017.
17. Wang, B.; Kostarelos, K.; Nelson, B.J.; Zhang, L. Trends in micro-/nanorobotics: Materials development, actuation, localization, and system integration for biomedical applications. *Adv. Mater.* **2021**, *33*, 2002047. [[CrossRef](#)]
18. Lauga, E. Life at high Deborah number. *EPL (Europhys. Lett.)* **2009**, *86*, 64001. [[CrossRef](#)]
19. Raz, O.; Avron, J.E. Swimming, pumping and gliding at low Reynolds numbers. *New J. Phys.* **2007**, *9*, 437. [[CrossRef](#)]
20. Hatton, R.L.; Choset, H. Geometric swimming at low and high Reynolds numbers. *IEEE Trans. Robot.* **2013**, *29*, 615–624. [[CrossRef](#)]
21. Alouges, F.; DeSimone, A.; Giraldo, L.; Zoppello, M. Self-propulsion of slender micro-swimmers by curvature control: N-link swimmers. *Int. J. Non-Linear Mech.* **2013**, *56*, 132–141. [[CrossRef](#)]
22. Wiesel, O.; Or, Y. Optimization and small-amplitude analysis of Purcell’s three-link microswimmer model. *Proc. R. Soc. Math. Phys. Eng. Sci.* **2016**, *472*, 20160425. [[CrossRef](#)]
23. Kadam, S.; Joshi, K.; Gupta, N.; Katdare, P.; Banavar, R. Trajectory tracking using motion primitives for the Purcell’s swimmer. In Proceedings of the 2017 IEEE/RSJ International Conference on Intelligent Robots and Systems (IROS), Prague, Czech Republic, 27 September–1 October 2017; pp. 3246–3251.
24. Kadam, S.; Banavar, R. Geometry of locomotion of the generalized Purcell’s swimmer: Modelling, controllability and motion primitives. *IFAC J. Syst. Control* **2018**, *4*, 7–16. [[CrossRef](#)]
25. Kósa, G.; Jakab, P.; Hata, N.; Jólesz, F.; Neubach, Z.; Shoham, M.; Zaaroor, M.; Székely, G. Flagellar swimming for medical micro robots: Theory, experiments and application. In Proceedings of the 2nd IEEE RAS & EMBS International Conference on Biomedical Robotics and Biomechatronics (BioRob 2008), Scottsdale, Arizona, 19–22 October 2008; pp. 258–263.
26. Abadi, A.; Kosa, G. Piezoelectric beam for intrabody propulsion controlled by embedded sensing. *IEEE/ASME Trans. Mechatronics* **2016**, *21*, 1528–1539. [[CrossRef](#)]
27. Mancha, E.; Traver, J.E.; Tejado, I.; Prieto, J.; Vinagre, B.M.; Feliu, V. Artificial Flagellum Microrobot. Design and Simulation in COMSOL. In *ROBOT 2017: Third Iberian Robotics Conference*; Ollero, A., Sanfeliu, A., Montano, L., Lau, N., Cardeira, C., Eds.; Springer International Publishing: Cham, Switzerland, 2018; pp. 491–501.
28. Traver, J.E.; Tejado, I.; Nuevo-Gallardo, C.; López, M.A.; Vinagre, B.M. Performance study of propulsion of N-link artificial eukaryotic flagellum swimming microrobot within a fractional order approach: From simulations to hardware-in-the-loop experiments. *Eur. J. Control* **2021**, *58*, 340–356. [[CrossRef](#)]
29. Hariri, H.; Bernard, Y.; Razek, A. A traveling wave piezoelectric beam robot. *Smart Mater. Struct.* **2013**, *23*, 025013. [[CrossRef](#)]
30. Prieto-Arranz, J.; Traver, J.E.; López, M.A.; Tejado, I.; Vinagre, B.M. Study in COMSOL of the generation of traveling waves in an AEF robot by piezoelectric actuation. In Proceedings of the XXXIX Jornadas de Automática, Badajoz, España, 5–7 September 2018; pp. 748–755.
31. López, M.A.; Prieto, J.; Traver, J.E.; Tejado, I.; Vinagre, B.M.; Petráš, I. Testing non reciprocal motion of a swimming flexible small robot with single actuation. In Proceedings of the 19th International Carpathian Control Conference (ICCC 2018), Szilvásvárad, Hungary, 28–31 May 2018; pp. 312–317.
32. Wang, T.; Ren, Z.; Hu, W.; Li, M.; Sitti, M. Effect of body stiffness distribution on larval fish-like efficient undulatory swimming. *Sci. Adv.* **2021**, *7*, eabf7364. [[CrossRef](#)]
33. Dias, J.M.S. A Study on Bending Stiffness Characterization of Biohybrid Microrobots Using External Magnetic Actuation. Ph.D. Thesis, Universidade de Coimbra, Coimbra, Portugal, 2021.
34. Shahinpoor, M.; Kim, K.J. Ionic polymer metal composites: IV industrial and medical applications. *Smart Mater. Struct.* **2004**, *14*, 197–214. [[CrossRef](#)]
35. Shen, Q.; Wang, T.; Wen, L.; Liang, J. Modelling and fuzzy control of an efficient swimming ionic polymer-metal composite actuated robot. *Int. J. Adv. Robot. Syst.* **2013**, *10*, 350. [[CrossRef](#)]
36. Hubbard, J.J.; Fleming, M.; Palmre, V.; Pugal, D.; Kim, K.J.; Leang, K.K. Monolithic IPMC fins for propulsion and maneuvering in bioinspired underwater robotics. *IEEE J. Ocean. Eng.* **2013**, *39*, 540–551. [[CrossRef](#)]

37. Chen, Z.; Bart-Smith, H.; Tan, X. IPMC-actuated robotic fish. In *Robot Fish*; Springer: Berlin/Heidelberg, Germany, 2015; pp. 219–253.
38. Chen, Z. A review on robotic fish enabled by ionic polymer–metal composite artificial muscles. *Robot. Biomim.* **2017**, *4*, 1–13. [[CrossRef](#)]
39. Chen, Z.; Hou, P.; Ye, Z. Robotic fish propelled by a servo motor and ionic polymer-metal composite hybrid tail. *J. Dyn. Syst. Meas. Control* **2019**, *141*, 071001. [[CrossRef](#)]
40. Nemat-Nasser, S. Micromechanics of actuation of ionic polymer-metal composites. *J. Appl. Phys.* **2002**, *92*, 2899–2915. [[CrossRef](#)]
41. Pugal, D. Physics Based Model of Ionic Polymer Metal Composite Electromechanical and Mechano-electrical Transduction. Ph.D. Thesis, University of Nevada, Reno, NV, USA, 2012.
42. Chen, Z.; Tan, X. A control-oriented and physics-based model for ionic polymer–metal composite actuators. *IEEE/ASME Trans. Mechatronics* **2008**, *13*, 519–529. [[CrossRef](#)]
43. Caponetto, R.; Graziani, S.; Sapuppo, F.; Tomasello, V. An enhanced fractional order model of ionic polymer-metal composites actuator. *Adv. Math. Phys.* **2013**, *2013*, 717659. [[CrossRef](#)]
44. Brennen, C.; Winet, H. Fluid mechanics of propulsion by cilia and flagella. *Annu. Rev. Fluid Mech.* **1977**, *9*, 339–398. [[CrossRef](#)]
45. Happel, J.; Brenner, H. *Low Reynolds Number Hydrodynamics: With Special Applications to Particulate Media*, 1st ed.; Springer: Dordrecht, The Netherlands, 2012.
46. Hinch, E. Hydrodynamics at low Reynolds numbers: A brief and elementary introduction. In *Disorder and Mixing*; Springer: Dordrecht, The Netherlands, 1988; pp. 43–56.
47. Purcell, E.M. Life at low Reynolds number. *Am. J. Phys.* **1977**, *45*, 3–11. [[CrossRef](#)]
48. Lauga, E.; Eloy, C. Shape of optimal active flagella. *J. Fluid Mech.* **2013**, *730*, R1. [[CrossRef](#)]
49. Gray, J.; Hancock, G.J. The propulsion of sea-urchin spermatozoa. *J. Exp. Biol.* **1955**, *32*, 802–814. [[CrossRef](#)]
50. Lighthill, M.J. Note on the swimming of slender fish. *J. Fluid Mech.* **1960**, *9*, 305–317. [[CrossRef](#)]
51. Nemat-Nasser, S.; Li, J.Y. Electromechanical response of ionic polymer-metal composites. *J. Appl. Phys.* **2000**, *87*, 3321–3331. [[CrossRef](#)]
52. Farinholt, K.M. Modeling and Characterization of Ionic Polymer Transducers for Sensing and Actuation. Ph.D. Thesis, Virginia Tech, Blacksburg, VA, USA, 2005.
53. Caponetto, R.; Graziani, S.; Pappalardo, F.L.; Umana, E.; Xibilia, M.; Giamberardino, P.D. A scalable fractional model for IPMC actuator. In Proceedings of the 7th Vienna International Conference on Mathematical Modelling, Vienna, Austria, 5–7 February 2011; pp. 593–596.
54. Caponetto, R.; Dongola, G.; Fortuna, L.; Graziani, S.; Strazzeri, S. A fractional model for IPMC actuators. In Proceedings of the 2008 IEEE Instrumentation and Measurement Technology Conference, Victoria, BC, Canada, 12–15 May 2008; pp. 2103–2107.
55. Tejado, I.; Traver, J.E.; Prieto-Arranz, J.; López, M.Á.; Vinagre, B.M. Frequency domain based fractional order modeling of IPMC actuators for control. In Proceedings of the 2019 18th European Control Conference (ECC), Naples, Italy, 25–28 June 2019; pp. 4112–4117.
56. Valério, D.; Sá da Costa, J. Ninteger: A fractional control toolbox for Matlab. In Proceedings of the 1st IFAC Workshop on Fractional Differentiation and its Applications, Bourdeaux, France, 19–21 July 2004; pp. 2103–2107.
57. Barbosa, R.S.; Machado, J.A.T.; Ferreira, I.M. Tuning of PID controllers based on Bode’s ideal transfer function. *Nonlinear Dyn.* **2004**, *38*, 305–321. [[CrossRef](#)]
58. Monje, C.A.; Chen, Y.; Vinagre, B.M.; Xue, D.; Feliu-Batlle, V. *Fractional-Order Systems and Controls: Fundamentals and Applications*, 1st ed.; Springer: London, UK, 2010.
59. Arrieta, O.; Vilanova, R. Simple PID tuning rules with guaranteed Ms robustness achievement. *IFAC Proc. Vol.* **2011**, *44*, 12042–12047. [[CrossRef](#)]